

Two-dimensional kinetic analysis of a Hall thruster discharge with a null-magnetic point at the anode

A. Marín-Cebrián,¹ E. Ahedo,¹ and A. Domínguez-Vázquez²

¹⁾Department of Aerospace Engineering, Universidad Carlos III de Madrid, Leganés, Spain

²⁾Department of Mechanical, Thermal and Fluid Engineering, Universidad de Málaga, Málaga, Spain

(*Electronic mail: almarinc@pa.uc3m.es)

(Dated: 13 June 2025)

A two-dimensional axial-radial particle-in-cell model is used to analyze the electron response in a non-shielded 5kW class Hall thruster. Radial asymmetries in the plasma discharge are present due to the cylindrical thruster geometry and the magnetic topology. The applied magnetic field presents a near-null point at the anode, from which a magnetic separatrix (MS) is born. Downstream of the MS, the plasma response is standard for a magnetic lens topology and agrees well with previous studies. In contrast, upstream of the MS, the magnetic field is nearly axial and partially shields the lateral walls. The magnetized electrons cannot easily cross the MS and are channeled toward the near-null magnetic point at the anode. This leads to sharp changes in the bulk plasma properties, significantly decreasing particle and energy fluxes to the walls. The lack of electrons reaching the outer dielectric wall upstream of the MS leads to the collapse of the classical electron-repelling sheath structure in order to comply with the dielectric condition. Electrons in this region are heated, and their inertia becomes comparable to their thermal energy. Moreover, consistently with previous simulations assuming a radial magnetic field, the electron response differs from a collisional fluid in terms of wall interaction properties, heat flux, and finite Larmor radius effects.

I. INTRODUCTION

The complex physics involved in the Hall effect thruster (HET) plasma is still not fully understood¹, hindering the development of accurate and efficient models of the discharge. Currently, simulations of real thrusters rely mainly on axial-radial quasineutral hybrid models^{2–5} due to their good trade-off between computational cost and accuracy. These models treat heavy species (i.e. ions and neutrals) with a particle-in-cell (PIC) formulation and electrons as a drift-diffusive fluid. The standard electron fluid formulation assumes a (near) Maxwellian VDF⁶. However, the low collisionality in the HET channel prevents the plasma from reaching local thermodynamic equilibrium; and thus, standard fluid models can misrepresent some relevant phenomena⁷. In contrast, full PIC models are capable of resolving the plasma without making assumptions on the species VDF, and can enrich electron fluid models with valuable kinetic information.

The analysis of the electron dynamics with PIC models in scenarios with a purely radial magnetic field^{8–13} has revealed important differences with respect to standard fluid models. In particular: (1) the electron VDF departs largely from the Maxwellian, (2) plasma-wall interaction parameters can differ largely from classical theory, (3) the electron heat flux has a complex behavior and, in general, it cannot be described by a Fourier-type law, and (4) the pressure tensor is composed of a gyrotropic anisotropic part and small gyroviscous terms. Indeed, near the anode, gyroviscosity, and electron inertia (i.e. finite Larmor radius effects, FLR) are relevant in the azimuthal momentum equation, where dominant terms are two orders of magnitude smaller than those in the axial

momentum equation.

However, the magnetic field in real HETs is curved. A magnetic lens topology is used to reduce the detrimental plasma fluxes to the lateral walls and improve the thruster performance^{14–16}. Previous studies using 1D PIC models^{17,18} have discussed the effect of the magnetic field curvature on the plasma response. The kinetic solution shows a significant reduction in electron temperature anisotropy and a higher replenishment of the wall collectible electron VDF tail. Axial-radial 2D models overcome some of the inherent limitations of 1D models and are more appropriate to analyze scenarios with complex magnetic topologies. Although there have been previous works in the literature that afforded axial-radial 2D PIC simulation with a curved magnetic field topology^{19–22}, the analyses focused mainly on the ion species and gross thruster performance figures.

In this work, we use our 2D axial-radial PIC model (PICASO)¹³ to analyze the effect of the magnetic field curvature on the plasma response, with special emphasis on the electron dynamics. A 5 kW-class HET similar to a PPS5000^{23,24}, with a non-shielded magnetic topology is considered for this study. The magnetic field features a near-null magnetic point at the anode wall and partially shields the lateral walls of the annular channel in the near-anode region. Results include the analysis of the VDFs, macroscopic transport equations, and plasma-wall interaction magnitudes. It is shown that the peculiar magnetic topology yields an unconventional electron response in the near-anode region.

The article is structured as follows. Section II summarizes the main aspects of the kinetic model. Section III presents the macroscopic plasma response and

the species VDF. Plasma-wall interaction magnitudes are commented in section IV. Section V analyzes the continuity, momentum, and energy equations of electrons, revealing the leading contributions in the macroscopic transport equations. Section VI discusses the local plasma response near the anode. Finally, conclusions are gathered in Section VII. Preliminary results of this work were presented at the 38th International Electric Propulsion Conference²⁵.

II. THRUSTER CONFIGURATION AND KINETIC MODEL

Figure 1(a) shows the simulation domain, comprising the thruster channel and the near plume. The domain boundaries are defined by the metallic anode (A), the lateral dielectric thruster walls (W), and the downstream plume boundary, which acts as a cathode/neutralizer (N). The thruster chamber has a length of $L = 29$ mm, and inner and outer radii $r_{W1} = 54.5$ mm and $r_{W2} = 76.7$ mm. The channel mean radius is $r_M = 65.6$ mm. The plume extends up to two channel lengths along the axial direction, and approximately three channel widths along the radial direction. Previous simulations²⁵ have shown that the plume size is large enough not to modify the

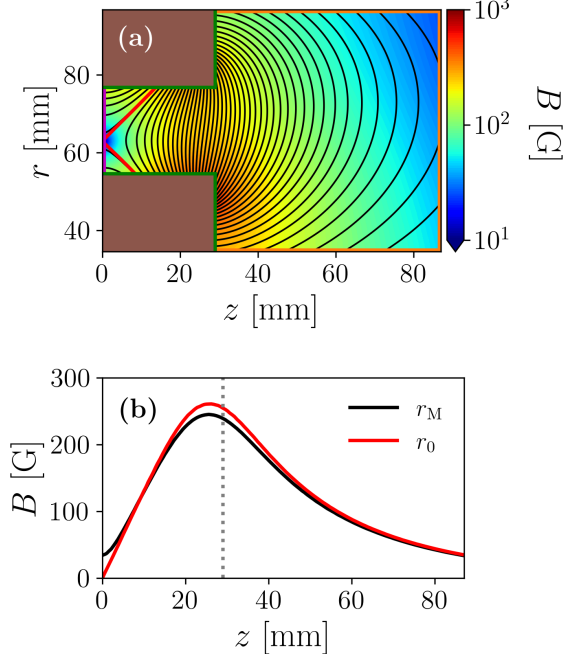


FIG. 1. Simulation domain and magnetic field topology. (a) 2D map of the magnitude of the applied magnetic field; magnetic field lines (—), the MS (—), the anode surface (A) (—), dielectric walls (W) (—), and the neutralizer/plume boundary (N) (—). (b) Axial profiles of $B = |\mathbf{B}|$ at $r = r_M = 65.6$ mm and at $r = r_0 = 62.9$ mm.

results inside the HET channel.

Figure 1(a) also depicts the 2D map of the magnitude of the applied, static magnetic field, \mathbf{B} . On the anode wall, at $r = r_0 = 62.9$ mm, there is a near-null point of the magnetic field (minimum $B = |\mathbf{B}|$ is 0.2 G), and from there a magnetic separatrix (MS) is born. The MS intersects the inner wall at $z \simeq 8.46$ mm, and the outer wall at $z \simeq 13.65$ mm. Thus, the MS separates the channel volume into three regions: the one downstream is rather conventional with a magnetic lens topology and B_r dominating; then there are two “triangular” regions between the MS and anode, with highly-curved magnetic lines, dominated by B_z , which intersect near perpendicularly the anode and confine magnetically the lateral walls. Cylindrical asymmetries are also evident in the magnetic field map. Axial profiles of B at $r = r_M$ and $r = r_0$ are plotted in Fig. 1(b).

In this work, the axisymmetric model PICASO¹³ simulates electrons (e) and singly-charged xenon ions (i) with a PIC formulation as two different populations of macroparticles with constant weight (i.e. number of elementary particles per simulated macroparticle). Explicit time integration of particle trajectories uses the Boris algorithm²⁶ and cylindrical effects on the particle motion are considered as described in Ref. 27. First-order weighting schemes (Cloud-In-Cell) are used for both, interpolating the magnetic and electric field to the particle position, and calculating the velocity distribution function (VDF) of each species as well as their macroscopic magnitudes.

The main macroscopic magnitudes of interest for species s are the density n_s , the particle flux vector $n_s \bar{\mathbf{u}}_s$, the momentum flux tensor \bar{M}_s , and the energy flux vector $\bar{\mathbf{P}}_s''$, defined as

$$\begin{aligned} n_s &= \iiint f_s d^3 v, & n_s \bar{\mathbf{u}}_s &= \iiint \bar{\mathbf{v}} f_s d^3 v, \\ \bar{M}_s &= m_s \iiint \bar{\mathbf{v}} \bar{\mathbf{v}} f_s d^3 v, & \bar{\mathbf{P}}_s'' &= \frac{m_s}{2} \iiint \bar{\mathbf{v}} \bar{\mathbf{v}}^2 f_s d^3 v. \end{aligned} \quad (1)$$

Other related macroscopic magnitudes are the current density vector $\mathbf{j}_s = e Z_s n_s \bar{\mathbf{u}}_s$, the pressure tensor $\bar{\bar{p}}_s = \bar{M}_s - m_s n_s \bar{\mathbf{u}}_s \bar{\mathbf{u}}_s$, the directional temperatures $T_{xs} = p_{xxs}/n_s$ for $x = z, r, \theta$, and the scalar temperature $T_s = \text{trace}(\bar{\bar{p}}_s)/(3n_s)$.

Since our main focus is electron dynamics, in order to limit the computational cost, we avoid simulating the slow dynamics of neutrals (n). Following Ref. 13, we model the neutral density with the simplified depletion law,

$$n_n(z) = \frac{\dot{m} - \dot{m}_{zi}(z)}{u_{zn} A m_i}, \quad (2)$$

where m_i is the ion mass, A is the channel cross-section area, u_{zn} is the (constant) neutral axial fluid velocity, $\dot{m}_{zi}(z)$ is the axial ion mass flow (computed at each axial section of the thruster) and \dot{m} is the injected neutral

mass flow through the anode. Equation (2) conserves the total mass flow and accounts for both, volumetric ionization and recombination of ions reaching the thruster walls. This approach avoids neutral dynamics, such as the breathing mode, and can be considered valid if the plasma response is steady-state.

Elastic, excitation, and ionization collisions of electrons with neutrals are treated with standard Monte Carlo Collision (MCC) algorithms. Ion collisions are quite marginal inside the thruster and are neglected in this work. Collisional cross-sections are retrieved from the Biagi database available in LXCat²⁸. Due to the axial-radial nature of the simulation, azimuthal instabilities inducing cross-field electron transport cannot be resolved. Instead, an empirical diffusive model is implemented through an isotropic anomalous electron collisionality of the form $\nu_{ano} = \alpha_{ano} \omega_{ce}$, with $\omega_{ce} = eB/m_e$ the electron cyclotron frequency and α_{ano} a two-parameter step function.

Electron and ion particles reaching any domain boundary contribute to the electric current there and are then removed from the simulation. The anode and cathode are connected through a power source setting a constant voltage bias V_d and with a (time-dependent) discharge current $I_d(t)$. At any instant, electrons are uniformly injected through the cathode surface, sampled from a Maxwellian flux VDF with a mean energy of 4.5 eV, such that the instantaneous net electric current at the anode and cathode are the same. Secondary electron emission (SEE) from the dielectric walls is taken into account, following the linear SEE yield

$$\delta_s(\mathcal{E}_{eWt}) = \mathcal{E}_{eWt}/\mathcal{E}_c, \quad (3)$$

with \mathcal{E}_{eWt} the impacting electron energy and \mathcal{E}_c the material cross-over energy. In the simulations here: $\mathcal{E}_c = 50$ eV and secondary electrons are sampled from a Maxwellian flux VDF with an average energy of 0.4 eV.

In the electrostatic approximation the electric field is $\mathbf{E} = -\nabla\phi$ and the electric potential, ϕ , is obtained from the Poisson equation

$$\frac{\partial^2\phi}{\partial z^2} + \frac{\partial^2\phi}{\partial r^2} + \frac{1}{r}\frac{\partial\phi}{\partial r} = \frac{e(n_e - n_i)}{\varepsilon}, \quad (4)$$

where ε is the electric permittivity and n_e , n_i are the electron and ion densities respectively. Dirichlet conditions are imposed at the cathode and anode, $\phi_N = 0$ and $\phi_A = V_d$, and Neumann conditions are applied at the dielectric walls,

$$\varepsilon\mathbf{E} \cdot \mathbf{1}_n = \sigma(t) \equiv - \int_0^t \mathbf{j} \cdot \mathbf{1}_n dt, \quad (5)$$

where: $\mathbf{1}_n$ is the unit vector perpendicular to the surface and pointing towards the plasma, σ is the surface charge density, and \mathbf{j} is the electric current density. At the steady-state Eq. (5) yields a local zero current at the dielectric walls. The numerical implementation of Eq.

(4) makes use of second-order finite differences schemes for the calculation of ϕ and \mathbf{E} at the mesh nodes.

The strict numerical constraints on the cell size and time step imposed by the Debye length and the inverse plasma frequency, respectively, are relaxed by using an augmented permittivity $\varepsilon = f_D^2 \varepsilon_0$, where ε_0 is the vacuum permittivity. This allows a reduction of the computational cost by a factor f_D^3 without a significant distortion of the steady-state solution as long as the Debye length remains the smallest length scale of the problem¹³.

A single operation point with $V_d = 300$ V, $m = 17.59$ mg/s, and $u_{zn} = 300$ m/s is simulated. Empirical parameters for the anomalous transport model were taken from Ref. 29. The numerical simulation presented here uses $f_D = 12$, a value aligned with previous works in the literature^{19,21}. For $n_e = 3 \cdot 10^{18}$ m⁻³, $T_e = 20$ eV, and $B = 250$ G as typical values, the following characteristic plasma magnitudes are computed: (augmented) Debye length $\lambda_{De} = 230$ μm; electron Larmor radius, $\rho_e = 681$ μm; (augmented) inverse plasma frequency $\omega_{pe}^{-1} = 123$ ps; and inverse electron gyrofrequency, $\omega_{ce}^{-1} = 227$ ps. The domain discretization uses a mesh with square cells with a length of 200 μm. The PIC time-step is $\Delta t = 15$ ps and the total simulated time is 60 μs (i.e. 4 million timesteps). The effect of the numerical parameters on the plasma solution is addressed in the Appendix, confirming the robustness of the results. Simulations were run on a workstation with 2 sockets, each one with 20 cores Intel(R) Xeon(R) Gold 6230 CPU @ 2.10 GHz. Using 20 cores, the reference simulation took approximately 169h.

III. FIRST SIMULATION RESULTS

The simulation starts with the domain uniformly filled with Maxwellian VDFs of ions and electrons, with densities and temperatures $n_{e0} = n_{i0} = 4 \cdot 10^{17}$ m⁻³ and $T_{e0} = T_{i0} = 1$ eV. During the initial transient, electrons and ions reaching the walls build up the surface charge

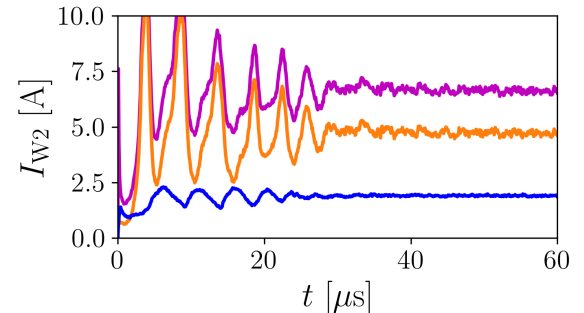


FIG. 2. Time evolution of the electron and ion currents to the outer wall: ions reaching the wall, $|I_{iW2}|$ (blue), electrons reaching the wall, $|I_{eW2t}|$ (purple), and electrons emitted from the wall (SEE), $|I_{eW2f}|$ (orange).

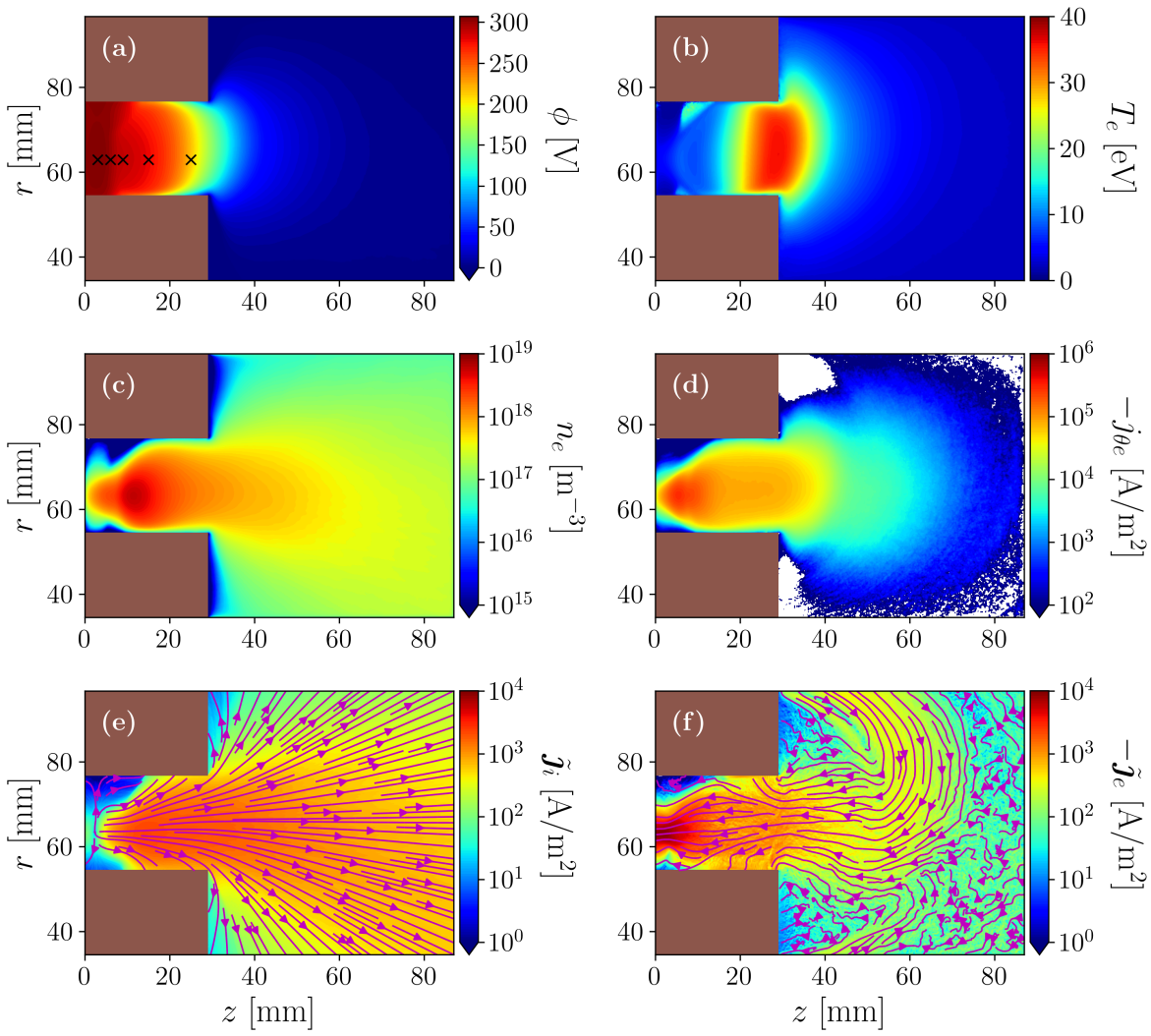


FIG. 3. Maps of the main macroscopic variables characterizing the discharge at steady-state: (a) electric potential, (b) electron scalar temperature, (c) electron density, (d) azimuthal electron current, (e) and (f) longitudinal ion and electron current densities respectively. Markers in plot (a) indicate the location of the electron and ion VDFs in Figs. 4 and 5.

density according to Eq. (5). Debye sheaths develop until the electric current to the wall becomes zero. The surface charge and the sheath stabilize after $\sim 0.5 \mu\text{s}$. Other transient processes related to ion dynamics and described in Ref. 13 follow until the steady state is reached at about $40 \mu\text{s}$. Figure 2 illustrates the transient period with the global currents at the outer dielectric wall. Hereon, only the stationary plasma response is shown and discussed. To mitigate the PIC-related noise, the plotted results are time-averaged values over the last $7.5 \mu\text{s}$ of the simulation (i.e. half a million time-steps). At steady state, the number of simulated particles per species, N_p , is over one million.

Figure 3 shows 2D maps of the main macroscopic plasma magnitudes. Three regions can be distinguished: (1) the near-plume region outside the thruster, (2) the

thruster near-exit region, and (3) the thruster near-anode region. The first notable feature in the maps is the presence of cylindrical asymmetries, arising from both, the geometry and the magnetic configuration; see, for instance, the ion and electron longitudinal currents in the plume (for vector magnitudes, such as $\tilde{\mathbf{j}}_e$, the longitudinal part is defined as $\tilde{\mathbf{j}}_e = \mathbf{j}_e - j_{\theta e} \mathbf{1}_\theta$). In this paper, the analysis focuses on the thruster channel plasma, which reveals significant differences between the regions upstream and downstream of the MS. The plasma magnitudes in the near-exit region are quite standard: a maximum T_e around the thruster exit; a maximum n_e inside the thruster, just when ϕ starts to decrease axially (thus accelerating ions); and a radial decay of ϕ . On the contrary, the near-anode region presents peculiar and complex features that we will analyze in detail in Section VI.

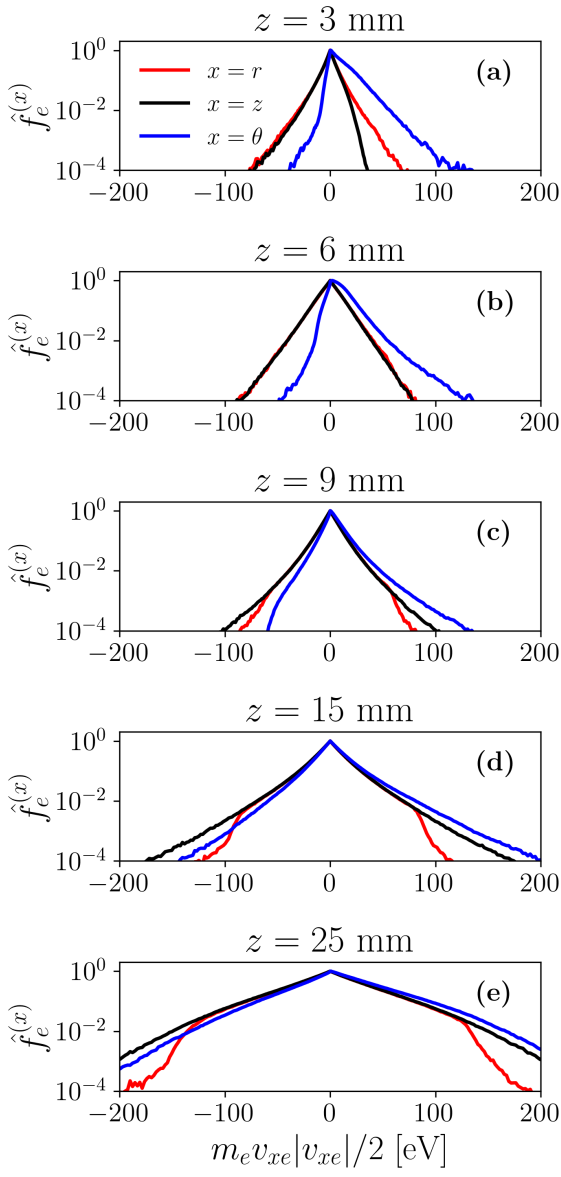


FIG. 4. Electron VDFs at $r = r_0$ and different axial locations inside the HET channel, marked in Fig. 3(a).

Moving to the kinetic description, Fig. 4 plots the normalized 1D electron VDFs at $r = r_0$ and different axial positions inside the HET channel. These 1D VDFs are defined as

$$\hat{f}_e^{(z)}(v_z) = \int_{-\infty}^{\infty} f_e(\mathbf{v}) dv_r dv_{\theta} \quad (6)$$

and similarly for $\hat{f}_e^{(r)}(v_r)$ and $\hat{f}_e^{(\theta)}(v_{\theta})$. The plots use the directional electron energy in the horizontal axis and a logarithmic scale in the vertical axis. Therefore, a Maxwellian VDF yields a line with a constant slope, and the wider the VDF, the higher the directional temperature. The relative shapes of the VDFs in Fig. 4 illustrate

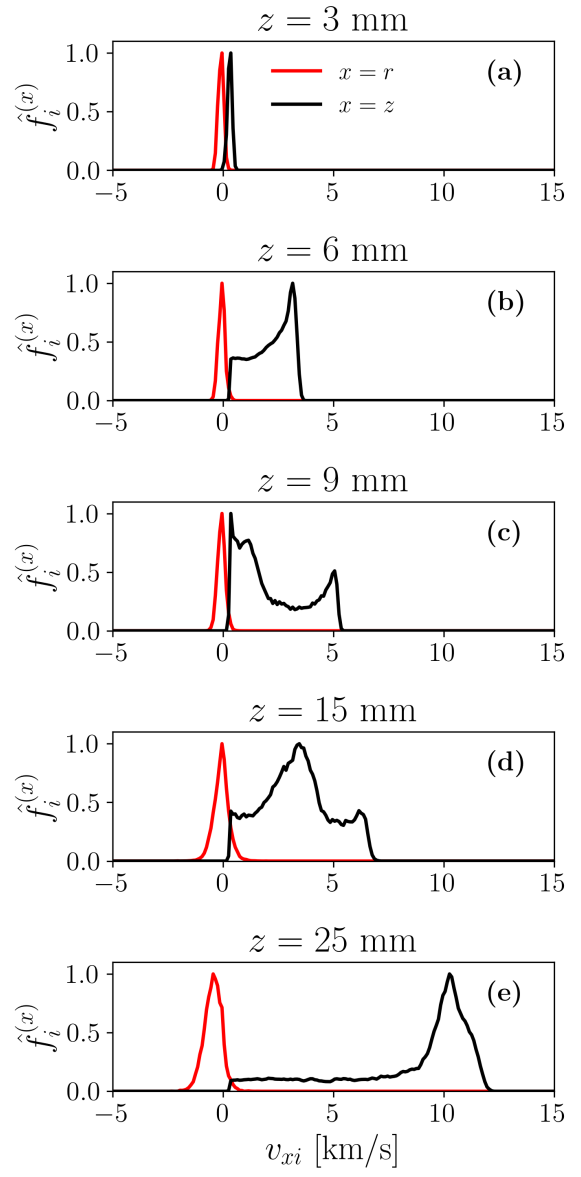


FIG. 5. Ion VDFs at $r = r_0$ and different axial locations inside the HET channel, marked in Fig. 3(a).

the axial decrease of T_e from channel exit to anode, in agreement with Fig. 3(b). The resulting electron VDF behavior differs depending on the thruster region. Near the thruster exit, at $z = 25$ mm at $z = 15$ mm, the axial and azimuthal VDF are almost identical with an approximately linear slope, yielding $T_{ze} \simeq T_{\theta e}$. The weak asymmetry between $\hat{f}_e^{(z)}$ and $\hat{f}_e^{(\theta)}$ is due to $u_{ze} \ll u_{\theta e} \ll c_e$. The high energy tails of the radial VDF are depleted due to wall collection and the weak electron collisionality. This reduces the radial temperature and leads to temperature anisotropy with $T_{re} < T_{ze} \simeq T_{\theta e}$. Qualitatively, this result is identical to those obtained from previous 1Dr models of the acceleration region of the

discharge^{11,30} assuming a purely radial magnetic field. As we move towards the central part of the channel, the magnetic curvature increases. At $z = 9$ mm it can be observed a higher replenishment of the radial VDF. This result is in agreement with previous works with 1D models accounting for the magnetic field curvature^{17,18}, which explained this effect due to the larger mixing between the radial and axial components of the velocity as a consequence of the magnetic field shape. At $z = 6$ mm the low wall losses [see Section IV] and high curvature of the magnetic field leads to $\hat{f}_e^{(r)}$ not presenting depleted tails. The larger asymmetry between $\hat{f}_e^{(\theta)}$ and $\hat{f}_e^{(z)} \simeq \hat{f}_e^{(r)}$ is the signature of $u_{\theta e}$ approaching c_e . Close to the anode, at $z = 3$ mm, an asymmetric $\hat{f}_e^{(z)}$ can be observed, with more electrons traveling with $v_z < 0$ than in the opposite direction. This is a consequence of the collection of electrons by the anode wall, as previously observed in Ref. 13, which leads to a lower T_{ze} .

Figure 5 depicts the normalized VDFs of ions. The kinetic response of the nearly unmagnetized and collisionless ions is very different from that of magnetized electrons. Ions are generated via $e - n$ ionization events and are then accelerated by the electric field. Since ions do not present an $\mathbf{E} \times \mathbf{B}$ azimuthal drift and $E_\theta = 0$ in the axisymmetric approximation, all ions have $v_\theta \simeq 0$ and $\hat{f}_i^{(\theta)}(v_\theta)$ resembles a Dirac delta function. Regarding $\hat{f}_i^{(r)}(v_r)$, it is near-Maxwellian with a small temperature T_{ri} . On the contrary, in no place $\hat{f}_i^{(z)}$ resembles an axially-drifted Maxwellian VDF: $\hat{f}_i^{(z)}(v_z)$ tends to become monoenergetic near the channel exit, while in the interior we detect the presence of slow new-born ions and partially accelerated ions. Depending on the relative relevance of these two effects, two-peak VDFs can be found, as observed at $z = 9$ mm. The large dispersion in ion velocities along z explains $T_{zi} > T_{ri}$.

IV. PLASMA-WALL INTERACTION

Figures 6(a) and 6(b) depict radial profiles of the (normalized) electric potential and plasma density at different axial locations (throughout the paper a single overbar on a variable means a radially-averaged value and subscript M refers to its value at $r = r_M$). Radial profiles near the thruster exit resemble those obtained with a 1Dr PIC model of the discharge with a purely radial magnetic field^{11,30}. Moving to inner thruster locations, n_e presents larger radial gradients and reaches lower values near the walls, as found in Ref. 18 for a magnetic lens configuration ($\alpha_B < 0$). In all sections, the maximum plasma density is shifted towards $r \simeq r_0$. The radial profiles of ϕ at $z = 25$ and 15 mm present the classical distinction between the quasineutral bulk of plasma and classical (i.e. electron repelling) sheaths, with much larger potential gradients, next to each dielectric wall. This is not the case for the innermost sections, at $z = 9, 6$, and 3 mm: the inner wall maintains a sizable sheath at $z = 9$

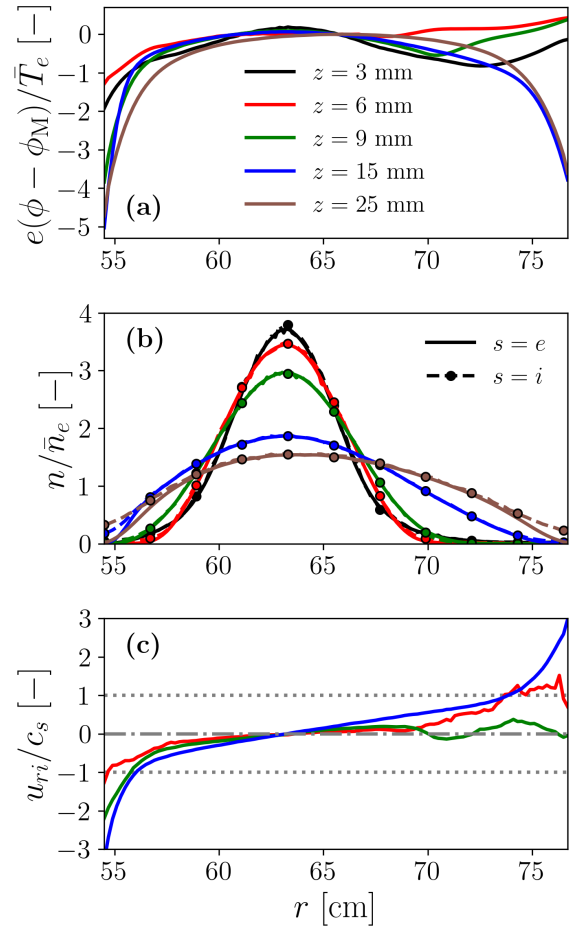


FIG. 6. Radial profiles of steady-state macroscopic variables for the reference case simulation at different axial locations: (a) non-dimensional electric potential, (b) non-dimensional ion and electron densities, and (c) non-dimensional ion radial velocity.

mm and a very reduced one at $z = 6$ and 3 mm. On the contrary, near the outer wall, ϕ grows from the bulk plasma towards the wall with mild $|\partial\phi/\partial r|$; and the classical sheath structure vanishes. The transition between the quasineutral plasma and the Debye sheath is typically considered at the position where the ion velocity normal to the wall becomes sonic (i.e. $c_s = \sqrt{T_e/m_i}$). Figure (c) plots the (normalized) radial ion velocity profiles at $z = 15, 9, 6$ mm, showing an unconventional shape close to the outer wall where the classical sheath structure collapses. The complex plasma behavior in this region will be further analyzed in Sec. VI.

Figure 7 depicts wall interaction magnitudes at the inner wall for electrons and ions. The ion current density to the wall, $|j_{riW}|$, the electron current density to the wall, $|j_{reWt}|$, and the electron current density emitted from the wall (SEE), $|j_{reWf}|$ are shown in Fig. 7(a). At any point, the local zero-current condition is satisfied, i.e. $|j_{riW}| = |j_{reWt}| - |j_{reWf}| = |j_{reW}|$. Ion, electron,

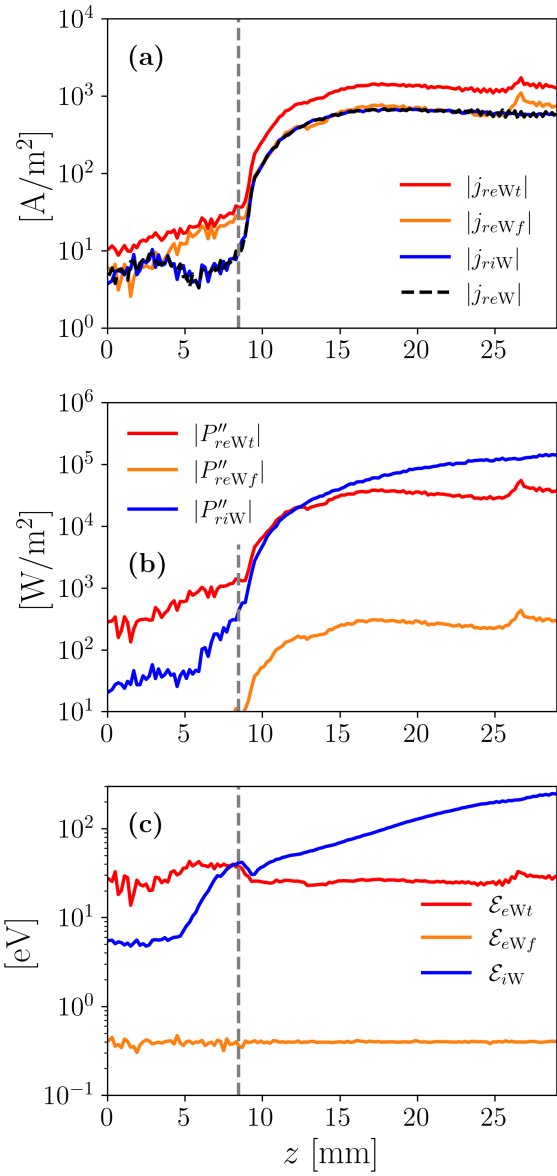


FIG. 7. Wall interaction magnitudes at the inner wall: (a) current densities, (b) energy fluxes, and (c) mean impact/emission energy. The dashed vertical line indicates the location where the MS intersects the inner dielectric wall.

and SEE energy fluxes, $|P''_{riW}|$, $|P''_{reWt}|$, and $|P''_{reWf}|$, respectively, are depicted in Fig. 7(b). Both, current and energy fluxes to the wall, suffer a sharp drop at the location where the MS intersects the wall. Similar results are found at the outer wall (not shown). At the inner wall, the average ion current density upstream of the MS is 6 A/m^2 , while downstream it is 522 A/m^2 . At the outer wall, we obtain 0.2 A/m^2 and 256 A/m^2 . Thus, the effect of the MS is stronger at the outer wall and leads to $|I_{iW1}| > |I_{iW2}|$ [see Table I]. Figure 7(c) plots the mean impact energies of ions and electrons, \mathcal{E}_{iW} and \mathcal{E}_{eWt} , respectively, and the mean energy of SEE, \mathcal{E}_{eWf} .

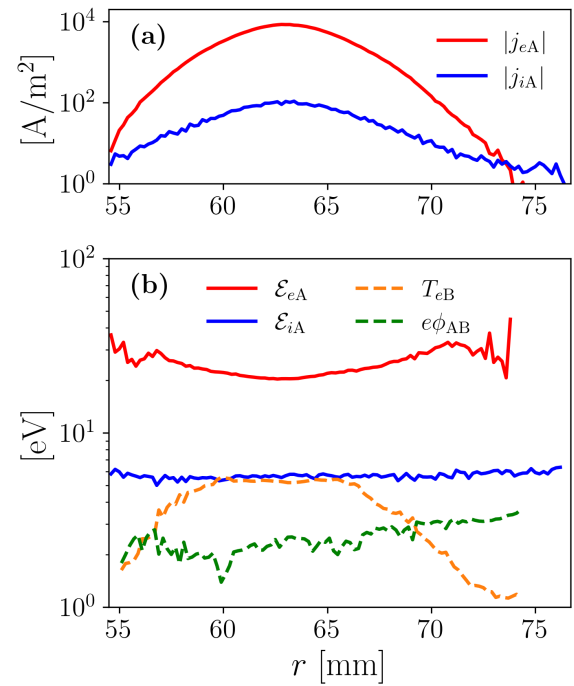


FIG. 8. Wall interaction magnitudes at the anode: (a) current densities, and (b) mean impact energies for electrons and ions. Plot (b) includes the scalar electron temperature at the ion sonic point B ($u_{z,iB} = -\sqrt{T_{eB}/m_i}$) and the potential drop $e\phi_{AB} = e(\phi_B - \phi_A)$.

Description and symbol	Value and units
Ion current to the anode, $ I_{iA} $	0.29 A
Electron current to the anode, $ I_{eA} $	18.71 A
Ion current to the inner wall, $ I_{iW1} $	3.71 A
Electron current to the inner wall, $ I_{eW1t} $	7.75 A
Ion current to the outer wall, $ I_{iW2} $	1.90 A
Electron current to the outer wall, $ I_{eW2t} $	6.52 A
Downstream ion beam current, $ I_{iN} $	15.89 A
Discharge power, $I_d V_d$	5527 W
Ion power to the anode, P_{iA}	2 W
Electron power to the anode, P_{eA}	404 W
Ion power to the inner wall, P_{iW1}	498 W
Net electron power to the inner wall, P_{eW1}	200 W
Ion power to the outer wall, P_{iW2}	264 W
Net Electron power to the outer wall, P_{eW2}	234 W
Downstream ion beam power, P_{iN}	3568 W

TABLE I. Current and power deposited at different surfaces.

The impact energy of ions, $\mathcal{E}_{iW} = e|P''_{riW}|/|j_{riW}|$, varies between $\sim 30 \text{ eV}$ at $z = 10 \text{ mm}$ and $\sim 200 \text{ eV}$ at the chan-

nel exit, thus having a big impact on wall erosion there. Conversely, the mean energy of primary electrons, i.e. $\mathcal{E}_{eWt} = e|P''_{reWt}|/|j_{reWt}|$ is rather uniform along each lateral wall: about 26 eV and 36 eV at the inner and outer walls respectively. Therefore, it deviates from the value of $2T_e$ [see Fig. 3(b)] corresponding to Maxwellian electrons. Similar results were obtained in Fig. 13 of Ref. 13 for a purely radial magnetic field, so this feature does not seem to be related to the magnetic curvature. The mean emission energy of SEE agrees with its target value, $\mathcal{E}_{eWF} = e|P''_{reWF}|/|j_{reWF}| \simeq 0.4$ eV. Since $\mathcal{E}_{eWF} \ll \mathcal{E}_{eWt}$, the net electron energy flux, $|P''_{reW}| = |P''_{reWt}| - |P''_{reWF}|$ corresponds almost entirely to $|P''_{reWt}|$ even in regions with intense SEE yield.

Figure 8 shows wall interaction magnitudes of ions and electrons at the metallic anode. The particle fluxes are maxima at the location where the separatrix intersects the anode, $r = r_0$. A classical electron-repelling Debye sheath is formed at the anode. Assuming that the ion sonic point, where $u_{zi} = -\sqrt{T_e/m_i}$, determines the anode sheath edge (B), the scalar electron temperature at B, T_{eB} ; and the sheath potential drop $e\phi_{AB} = e(\phi_B - \phi_A)$ are calculated in 8(b). The mild anode sheath (~ 3 V) justifies the low average ion impact energy at the anode, $\mathcal{E}_{iA} \simeq 6$ eV in Fig. 8(b). Electrons reach the anode with a higher energy, $\mathcal{E}_{eA} \simeq 20$ eV. This result differs from $2T_{eB}$ and is a consequence of the local features of the electron VDF near the anode (not shown), which reveals the presence of two main electron populations. First, there is a low-energy population coming from local ionization. Second, there is a tail of high-energy electrons directed towards the anode. The high-energy tail of the VDF presents a similar slope at different radial locations. This is in line with the relatively high and uniform electron impact energy at the anode wall.

Table I gathers the total currents and powers to the different boundaries in steady-state, obtained by integration of local values. Observe that the ion current to the anode is quite small, as desired, and the discharge current is $I_d = |I_{eA}| - |I_{iA}| \simeq 18.4$. The inner and outer walls present large asymmetries, as already anticipated. The inner wall, with 70% of the surface of the outer wall, receives almost twice the ion current. This result is consistent with the higher plasma density found in the vicinity of the inner wall in Figs. 3(c) and 6(b). The secondary electron currents from the lateral walls correspond to SEE effective yields of $\delta_{s1} \simeq 0.52$ and $\delta_{s2} \simeq 0.71$ (according with electron impact energies of 26 eV and 36 eV commented above).

V. MACROSCOPIC BALANCES

A. Continuity equation

The radially integrated steady-state current balance for electrons and ions can be expressed as

$$\frac{dI_{zs}}{dz} = \frac{dI_{prod}}{dz} - \frac{dI_{rs}}{dz}, \quad s = i, e, \quad (7)$$

with I_{zs} the axial current, dI_{prod}/dz the rate of current production, and dI_{rs}/dz the rate of current losses to the lateral walls. Figure 9(a) plots the different contributions to this balance. Near the anode, the plasma losses to the walls are very small; therefore, all the plasma production resulting from ionization contributes to the axial current. Conversely, near the thruster exit, ionization compensates plasma losses to the lateral walls and the axial current is approximately constant.

The 1Dz models of Refs. 31–33 describe lateral wall losses as

$$\frac{1}{A} \frac{dI_{rs}}{dz} = e\bar{n}_e \nu_w, \quad \nu_w = \tilde{\nu}_w \frac{2\pi r_M}{A} \sqrt{\frac{\bar{T}_e}{m_i}} \quad (8)$$

with \bar{n}_e the average plasma density in the cross section and ν_w an equivalent “wall-collision frequency”. In the 1Dz model, $\tilde{\nu}_w$ is a phenomenological parameter to be fitted, which is usually assumed constant; for instance Refs. 32 and 33 take $\tilde{\nu}_w = 0.17$ to obtain reasonable lateral losses. Figure 9(b) plots the local $\tilde{\nu}_w$ for this topology, which is ~ 1 in the near-exit region, and $\ll 1$ in the near-anode due to the grazing incidence of the magnetic field. It has been checked that with the fully-radial magnetic topology of Ref. 13, $\tilde{\nu}_w \sim 1$ all along the channel.

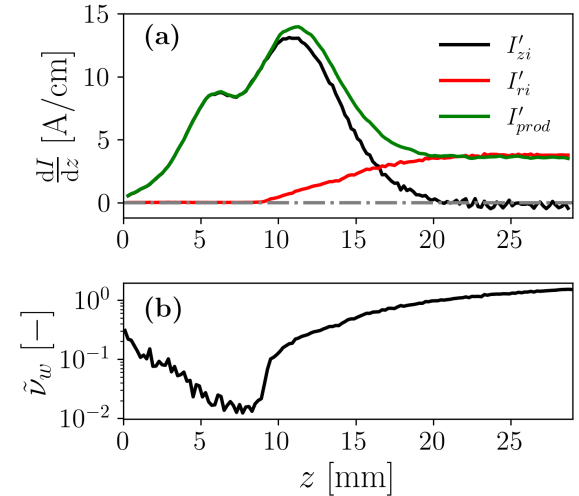


FIG. 9. Continuity equation: (a) contributions to the current balance [Eq. (7)] for the ion population (the notation $' \equiv d/dz$ is used in the legend); (b) non-dimensional wall collisionality parameter defined in Ref. 31.

1 **B. The electron momentum equation**

2 The radial momentum equation can be expressed as

3
$$0 \simeq -\frac{\partial p_{rre}}{\partial r} - en_e E_r + j_{\theta e} B_z, \quad (9)$$

4 since the remaining terms, including inertia, temperature
 5 anisotropy, and collisions are found to be negligible
 6 in the bulk plasma. Therefore, there is a balance among
 7 the pressure, electric, and magnetic forces, the last one
 8 due to the curvature of the magnetic field. The different
 9 terms of the balance are plotted in Fig. 10 at several axial
 10 sections of the HET channel. Notice first the change
 11 of sign of the forces around $r \approx r_0$ (except at $z = 25\text{mm}$
 12 for the magnetic force, which anyway is rather small).
 13 Except for this anomaly, we observe that at both sides
 14 of $r \approx r_0$, the pressure force has an expanding character
 15 (i.e pushing electrons towards the two lateral walls), while
 16 the electric and magnetic forces have a confining character;
 17 of these two, the magnetic force dominates near the anode
 18 and the electric force near the thruster exit.

19 The axial momentum equation can be approximated
 20 by the classical expression

21
$$0 \simeq -\frac{\partial p_{zze}}{\partial z} - en_e E_z - j_{\theta e} B_r, \quad (10)$$

22 stating that the azimuthal drift combines $E \times B$ and
 23 diamagnetic drifts. Collisional and $\partial M_{rze}/\partial z$ contributions
 24 are subdominant with respect to the strong axial
 25 electron pressure gradient and electric force. Figure 11
 26 plots this axial balance for radially-averaged variables,
 27 and shows also that axial electron inertia effects (i.e.
 28 $m_e n_e u_{ze}^2 = M_{zze} - p_{zze}$) are negligible. In fact, the
 29 plasma response close to the anode resembles that of an
 30 unmagnetized plasma, in which the pressure and electric
 31 force balance, and the magnetic force becomes small. The
 32 complex behavior in the near-anode region is responsible
 33 for the local extrema of the profiles at $z \sim 7\text{mm}$.

34 Finally, the azimuthal electron momentum equation
 35 reads

36
$$0 \simeq -\frac{\partial M_{z\theta e}}{\partial z} + j_{ze} B_r - j_{re} B_z + F_{col,\theta e}. \quad (11)$$

37 The term $\partial M_{z\theta e}/\partial z$, combining inertia and gyroviscous
 38 contributions, is a kinetic Finite-Larmor-Radius (FLR)
 39 effect^{34,35}. Figure 12 compares the radially averaged
 40 terms in Eq. (11). Observe first that the dominant terms
 41 are much smaller (typically 2 orders of magnitude) than
 42 in the axial momentum balance in Eq. (10). Near the
 43 thruster exit both $j_{re} B_z$ and $\partial M_{z\theta e}/\partial z$ are small, and
 44 the classical result $j_{ze} B_r \simeq -F_{col,\theta e}$ is retrieved. Con-
 45 versely, near the anode, all the terms in Eq. (11) become
 46 relevant. The relevance of FLR effects, particularly near
 47 the anode, is found in other 1D¹² and 2D³⁶ kinetic
 48 studies and also in our previous work¹³ where \mathbf{B} was
 49 purely radial. Finally, observe that Eq. (11) determines

50 $j_{\top e} = (j_{ze} B_r - j_{re} B_z)/B$, i.e. the current density perpen-
 51 dicular to \mathbf{B} (or cross-field current). This equation must
 52 be completed with the 2D electron continuity equation
 53 to determine j_{ze} and j_{re} individually. Only where B_z

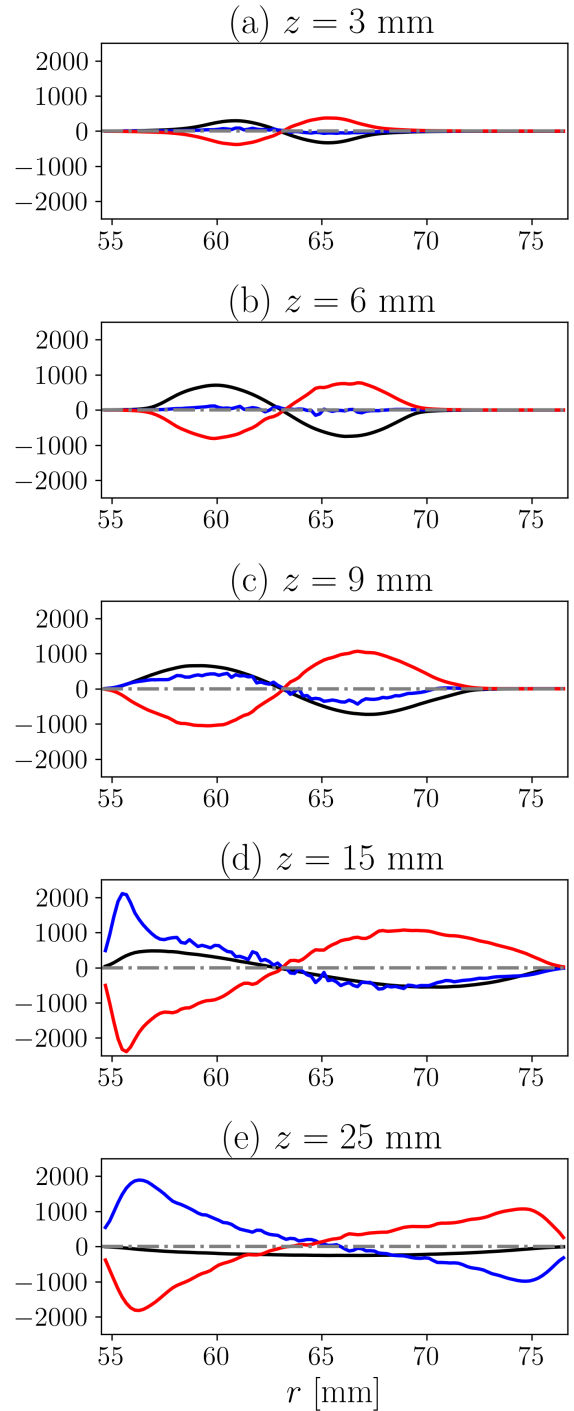


FIG. 10. Main contributions to the radial momentum balance, Eq. (9), at five different axial sections in N/m^3 : $-\partial p_{rre}/\partial r$ (—), $-en_e E_r$ (—), $j_{\theta e} B_z$ (—),

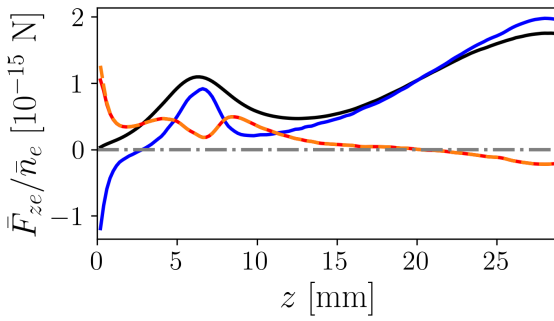


FIG. 11. Contributions to the (radially averaged) axial electron momentum balance [Eq. (10)]. In Fig. (a), the following axial forces, F_{ze} , are depicted: $-j_{\theta e}B_r$ (—), $e n_e E_z$ (—), $\partial M_{zze}/\partial z$ (—), and $\partial p_{zze}/\partial z$ (---).

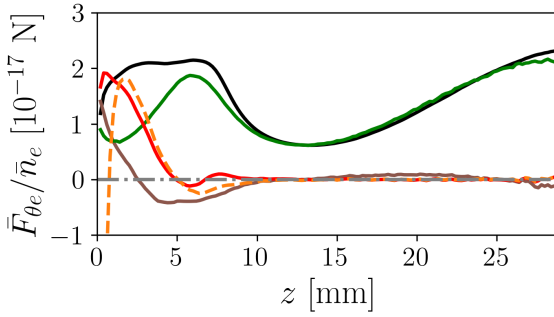


FIG. 12. Contributions to the (radially averaged) azimuthal electron momentum balance [Eq. (11)]. In Fig. (b), the following azimuthal forces, $F_{\theta e}$, are depicted: $j_{ze}B_r$ (—), $-j_{re}B_z$ (—), $-F_{col,\theta e}$ (—), $\partial M_{z\theta e}/\partial z$ (—), and $\partial p_{z\theta e}/\partial z$ (---).

is negligible, the cross-field current is the axial current, the one that defines the electron current collected by the anode.

C. The electron energy flux vector

The stationary electron energy equation is

$$\nabla \cdot \mathbf{P}_e'' = \mathbf{j}_e \cdot \mathbf{E} - P_{inel}''' \quad (12)$$

where \mathbf{P}_e'' is the electron energy flux vector, $\mathbf{j}_e \cdot \mathbf{E}$ the work of the electric field and P_{inel}''' the power spent in inelastic collisions. In a macroscopic formulation, the energy flux is commonly expressed as the sum of four different contributions:

$$\mathbf{P}_e'' = \mathbf{h}_e + \mathbf{q}_e + \mathbf{U}_e + \boldsymbol{\Pi}_e, \quad (13)$$

with $\mathbf{h}_e = (5/2)n_e T_e \mathbf{u}_e$ the enthalpy flux, \mathbf{q}_e the heat flux, $\mathbf{U}_e = m_e u_e^2 n_e \mathbf{u}_e / 2$ the flux of kinetic energy of the

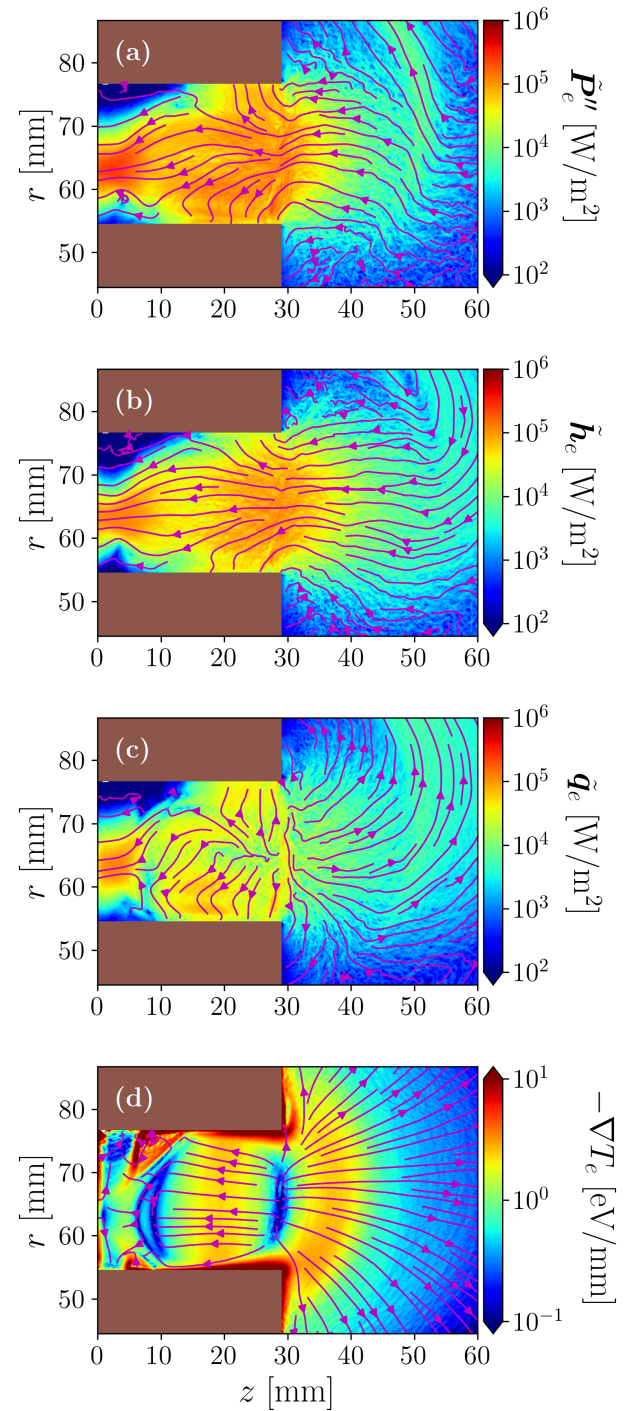


FIG. 13. The electron energy flux vector: (a) total electron energy flux vector, (b) enthalpy flux vector, (c) heat flux vector, and (d) electron temperature gradient.

fluid flow and $\boldsymbol{\Pi}_e = (\bar{p}_e - p_e \bar{I}) \cdot \mathbf{u}_e$ the energy flux coming from anisotropic and non-gyrotropic features of the pressure tensor.

Fig. 13(a) plots the longitudinal electron energy flux

vector, $\tilde{\mathbf{P}}_e''$, computed from the PIC results. The analysis of the different terms in Eq. (13) reveals that contributions from both $\tilde{\mathbf{U}}_e$ and $\tilde{\mathbf{\Pi}}_e$ are negligible except near the MS due to large electron inertia. Thus, they are omitted in Fig. 13. The main contributors to the electron energy flux vector are shown in Fig. 13(b) and (c). The enthalpy flux vector constitutes the dominant contribution to $\tilde{\mathbf{P}}_e''$ inside the thruster. The subdominant contribution comes from $\tilde{\mathbf{q}}_e$, which axially points towards the anode as \mathbf{h}_e . In the near plume $\tilde{\mathbf{h}}_e$ and $\tilde{\mathbf{q}}_e$ compete and tend to point in different directions. At the thruster exit, where T_e reaches its maximum value, $\tilde{\mathbf{q}}_e$ changes sign. This suggests a dependence with ∇T_e and thus a classical conductive response. In an attempt to establish a correlation, ∇T_e is computed in Fig. 13(d). However, the behavior of $\tilde{\mathbf{q}}_e$ is too complex to be amenable to a simple law, and hence the same happens with $\tilde{\mathbf{P}}_e''$.

VI. ANALYSIS OF THE NEAR-ANODE REGION

In order to analyze the complex plasma response near the anode, Fig. 14 zooms in the region that extends from the anode to $z = 15$ mm. The magnetic field has a strong influence on the plasma behavior, and the MS acts as a boundary between the different regions. As shown in Fig. 1, downstream of the MS, the magnetic field presents a conventional magnetic lens topology; while upstream of the MS, the magnetic field features a large curvature and partially shields the lateral dielectric walls.

Figure 14(f) plots the longitudinal electron current density with streamlines. It shows that once the electron flow reaches the MS it follows the most electrically favorable path (i.e. along the MS) and reaches the anode around the near-null point. This prevents most of the magnetized electrons from reaching the region upstream of the MS. Consequently, the electron density presents a sharp jump across the MS, as shown in Fig. 14(a). This effect is stronger near the outer wall because it is farther away from the null point, and thus \mathbf{B} is stronger there. The lateral walls of the thruster are dielectric, and therefore, at steady-state, they cannot collect net electric current from the plasma, i.e. $|j_{rew}| = |j_{riw}|$. Since the electron current to the wall is so small in this region, very few ions must reach the wall. The current of unmagnetized ions, in Fig. 14(e), is controlled by the combined action of ion production and the electric field. The electric potential ϕ and its gradient \mathbf{E} self-adjust to achieve the appropriate response of electrons and ions. The most unconventional feature is that the electric potential grows from the plasma to the outer dielectric wall, as already anticipated in Fig. 6(a). This is contrary to the case of a classical electron-repelling sheath and leads to local electric field reversal (i.e. electron attracting and ion repelling), as shown in Fig. 14(d). The ion density, in Fig. 14(b), tries to follow the electron density to keep the plasma quasineutral, but this fails in the triangles around the anode corners, where $n_i > n_e$.

Moving into electron energy considerations, the electric field work is the main source of energy for electrons [see Eq. (12)]. Fig. 14(g) shows the 2D map of power deposited by the electric field per electron particle, $j_e \cdot \mathbf{E}/n_e$. It presents very high relative values near the lateral walls, immediately upstream of the MS. These are due to a relatively mild change in both j_e and \mathbf{E} and the strong decrease in n_e . The consequence is a large increase of both, the electron thermal energy [see T_e in Fig. 14(h)], and the kinetic energy of the fluid flow [see $m_e u_e^2/2$ in Fig. 14(i)]. Indeed, $m_e u_e^2/2 \sim T_e$ in this region, breaking the drift-diffusive approximation there. The fluid electron velocity dominated by $u_{\theta e}$, suffers a steep change across the MS [see Fig. 14(j)]. The local analysis of the different terms in the axial momentum equation [Eq. (10), in Figs. 14(k) and (l)] reveals that the increase of $u_{\theta e}$ is mainly driven by the term $\partial p_{zze}/\partial z$; which becomes large due to the sharp change in n_e across the MS [in Fig. 14(a)].

VII. CONCLUSION

A 2D-3V axisymmetric PIC model has been used to discuss the effect of magnetic curvature on the kinetic plasma response in a HET, focusing mainly on the electron population behavior. The simulation code of Ref. 13 was applied to simulate a 5kW class Hall thruster similar to the PPS5000.

Consistently with our previous study for purely radial magnetic topology¹³ we find: (1) the mean electron energy to the walls does not correspond to $2T_e$; (2) the electron energy flux is mainly given by the enthalpy and the heat flux, the latter not following a simple Fourier law; (3) finite Larmor radius effects play an important role in the azimuthal electron momentum equation in the near anode region. Near the thruster exit, where the magnetic field is approximately radial, the high-energy tail of the radial electron VDF is largely depleted, as in Ref. 30. In the central region, with a moderately curved magnetic field, there is a higher replenishment of the VDF tails, in agreement with Ref. 18.

However, in the two “triangular” regions bounded by the MS and the anode, the response is unconventional. Upstream of the MS, the magnetic field partially shields the lateral walls of the channel and confines the electrons away from them. The plasma density is maximum around r_0 , the radial location of the near-null magnetic point at the anode wall, and decreases towards the lateral walls by two or three orders of magnitude. This implies a similar reduction in the electron current and energy fluxes to the walls. To comply with the local dielectric condition at the walls, the classical sheath structure collapses, and, instead, the electric potential grows from the bulk plasma to the wall attracting electrons and repelling unmagnetized ions. The power of the electric field on electrons in this region increases both, the thermal energy and the kinetic energy of the fluid flow. The latter

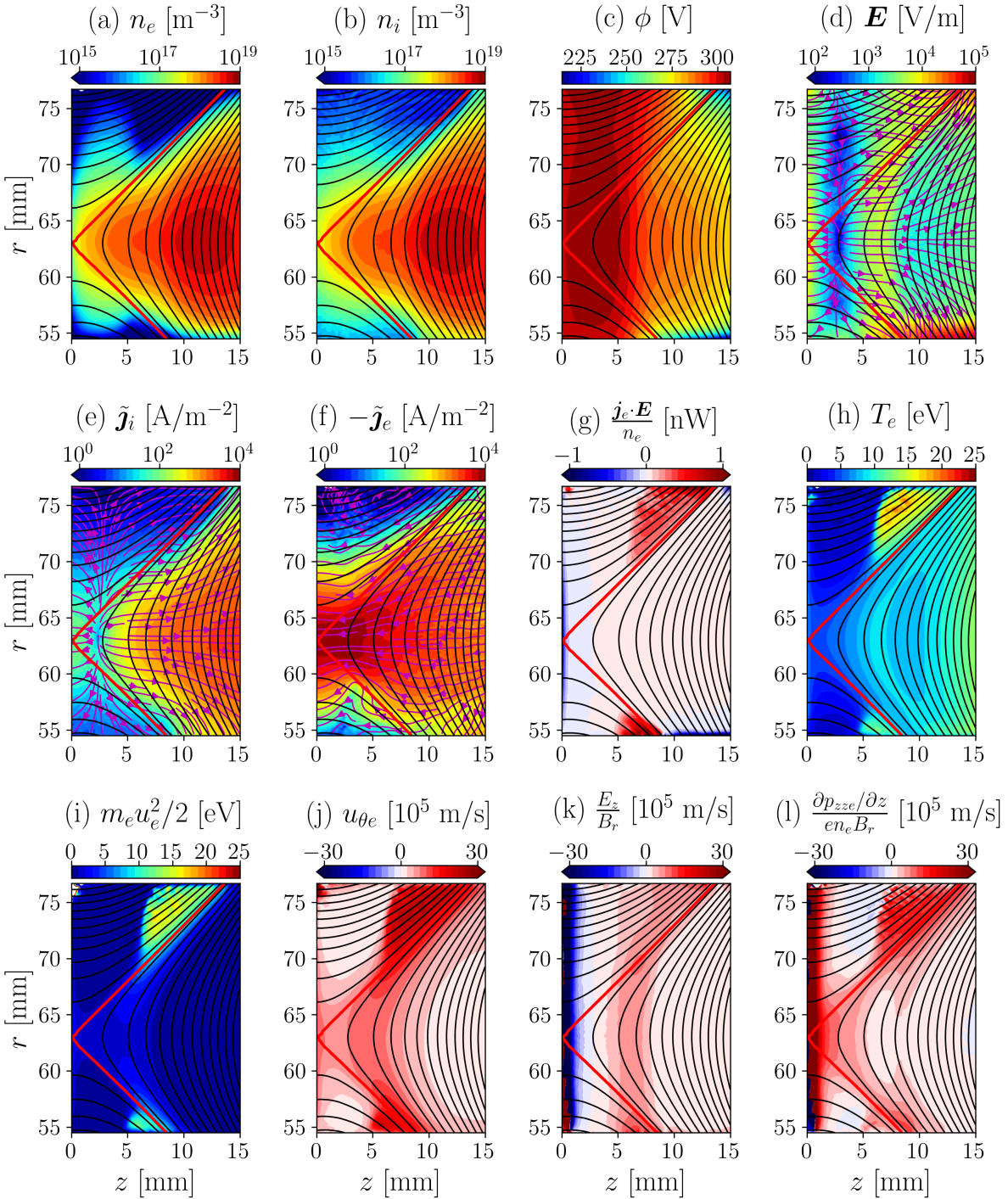


FIG. 14. Macroscopic plasma variables near the anode: (a) electron density, (b) ion density, (c) electric potential, (d) electric field, (e) longitudinal ion current density, (f) longitudinal electron current density, (g) power of the electric field on the electron population per unit particle, (h) scalar electron temperature, (i) kinetic energy of the electron fluid flow, (j) azimuthal electron velocity, (k) and (l) depict the main contributions to $u_{\theta e}$ from Eq. (10). Black contours represent magnetic field lines and the MS is plotted in red.

becomes comparable to the former, invalidating the drift-diffusive approximation.

The unconventional plasma response upstream of the

MS is a consequence of the low cross-field electron mobility. Therefore, a self-consistent characterization of this region requires a 3D kinetic description of the plasma

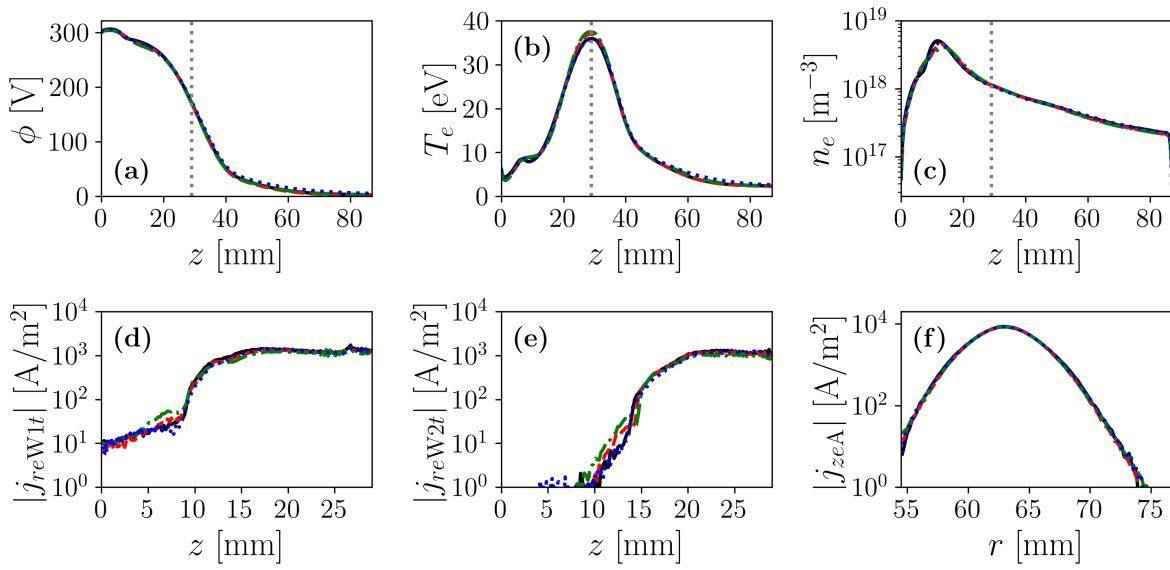


FIG. 15. Comparison of simulations with different numerical parameters [Reference (—), $2N_p$ (---), $4N_p$ (-·-), and $f_D = 8$ (.....)]. First row, axial profiles at r_M : (a) electric potential, (b) scalar electron temperature, and (c) electron density. Second row, electron current densities to different thruster surfaces: (d) inner wall, (e) outer wall, and (f) anode.

discharge, that takes into account azimuthal instabilities, wall collection, and axial plasma transport effects. Sheath reversal due to grazing magnetic incidence could also be present in magnetic shielding topologies, where the magnetic field is almost parallel to the walls. The analysis of such topologies will be addressed in a future publication.

ACKNOWLEDGMENTS

This work has been supported by the R&D project HEEP (PID2022-140035OB-I00) funded by MCIN/AEI/10.13039/501100011033 and by “ERDF A way of making Europe”. The authors thank E. Bello-Benítez for his contribution to the development of code.

EFFECT OF NUMERICAL PARAMETERS IN THE PLASMA SOLUTION

Additional simulations have been performed to verify the robustness of the numerical results. The effect of the domain size and time-step were addressed in Ref. 25. The simulated domain is large enough so that the results in the thruster channel are insensitive to the plume size. Moreover, results do not change if a smaller Δt is used. Here, we address the effect of the number of simulated particles, N_p , and the augmentation factor for the vacuum permittivity, f_D . For the different numerical experiments, axial profiles of macroscopic magnitudes at r_M and local electron current densities to different thruster

surfaces are provided in Fig. 15.

First, simulations that double and quadruple the number of simulated particles, N_p , keeping identical meshes, time-step, and f_D ; show the same trends as in the reference simulation. The small quantitative changes are an indication that N_p does not significantly affect the solution, and the results of the reference case are robust.

Second, we address the effect of the augmented vacuum permittivity. In Ref. 13, we found that simulations with $f_D = 5$ and 10 were almost indistinguishable, while a simulation with $f_D = 20$ presented larger deviations. In order to prove that the simulation results are not affected by our choice of $f_D = 12$, an additional test case, with $f_D = 8$, was simulated. The mesh size was reduced ($\Delta z = \Delta r = 100 \mu\text{m}$) and, consequently, the time-step was adjusted ($\Delta t = 10 \text{ ps}$). The number of particles per cell was set to be the same as in the reference case. The solutions in both cases are nearly identical, showing that the augmented Debye length has a weak effect on the simulation results within this range of f_D .

Inevitably, numerical thermalization is present in PIC simulations³⁷. In order to minimize its effects on the simulation results, it has to occur in time scales that are longer than other relevant phenomena affecting the electron VDF. Considering $f_D = 12$ and typical values for $n_e = 3 \cdot 10^{18} \text{ m}^{-3}$ and $T_e = 20 \text{ eV}$, the number of macroparticles per Debye volume is $N_D \simeq 100$, yielding a numerical thermalization equivalent frequency of $7.22 \cdot 10^6 \text{ s}^{-1}$. A characteristic value for the anomalous collision frequency is $5.29 \cdot 10^7 \text{ s}^{-1}$ and the inverse of the radial transit time of an electron is estimated as $\bar{c}_e/(r_{W2} - r_{W1}) \simeq 1.35 \cdot 10^8 \text{ s}^{-1}$. Therefore, other phe-

nomena dominate over numerical thermalization. This is further confirmed by the weak variation in the results shown in cases with a larger number of simulated particles, for which a lower numerical thermalization is expected.

REFERENCES

- ¹Igor D. Kaganovich, Andrei Smolyakov, Yevgeny Raitses, Eduardo Ahedo, Ioannis G. Mikellides, Benjamin Jorns, Francesco Taccogna, Renaud Gueroult, Sedina Tsikata, Anne Bourdon, Jean-Pierre Boeuf, Michael Keidar, Andrew Tasman Powis, Mario Merino, Mark Cappelli, Kentaro Hara, Johan A. Carlsson, Nathaniel J. Fisch, Pascal Chabert, Irina Schweigert, Trevor Lafleur, Konstantin Matyash, Alexander V. Khrabrov, Rod W. Boswell, and Amnon Fruchtman. Perspectives on physics of ExB discharges relevant to plasma propulsion and similar technologies. *Physics of Plasmas*, 27(12):120–601, 2020.
- ²J. M. Fife. *Hybrid-PIC modeling and electrostatic probe survey of Hall thrusters*. PhD thesis, Massachusetts Institute of Technology, 1998.
- ³E. Sommier, M.K. Scharfe, N. Gascon, M.A. Cappelli, and E. Fernandez. Simulating plasma-induced Hall thruster wall erosion with a two-dimensional hybrid model. *Plasma Science, IEEE Transactions on*, 35(5):1379–1387, 2007.
- ⁴A.L. Ortega, I.G. Mikellides, M.J. Sekerak, and B.A. Jorns. Plasma simulations in 2-d (r-z) geometry for the assessment of pole erosion in a magnetically shielded Hall thruster. *Journal of Applied Physics*, 125(3), 2019.
- ⁵Jesús Perales-Díaz, Adrián Domínguez-Vázquez, Pablo Fajardo, Eduardo Ahedo, Farbod Faraji, Maryam Reza, and Tommaso Andreussi. Hybrid plasma simulations of a magnetically shielded Hall thruster. *Journal of Applied Physics*, 131(10):103302, 2022.
- ⁶J.A. Bittencourt. *Fundamentals of plasma physics*. Springer, Berlin, Germany, 2004.
- ⁷E. Ahedo. Using electron fluid models to analyze plasma thruster discharges. *Journal of Electric Propulsion*, 2(1):2, 2023.
- ⁸F. Taccogna, S. Longo, and M. Capitelli. Plasma sheaths in Hall discharge. *Physics of Plasmas*, 12(9):093506, 2005.
- ⁹I.D. Kaganovich, Y. Raitses, D. Sydorenko, and A. Smolyakov. Kinetic effects in a Hall thruster discharge. *Physics of Plasmas*, 14:057104, 2007.
- ¹⁰F. Taccogna, R. Schneider, S. Longo, and M. Capitelli. Kinetic simulations of a plasma thruster. *Plasma Sources Science and Technology*, 17(2):024003, 2008.
- ¹¹Adrián Domínguez-Vázquez, Francesco Taccogna, and Eduardo Ahedo. Particle modeling of radial electron dynamics in a controlled discharge of a Hall thruster. *Plasma Sources Science and Technology*, 27(6):064006, 2018.
- ¹²Yusuke Yamashita, Raymond Lau, and Kentaro Hara. Inertial and anisotropic pressure effects on cross-field electron transport in low-temperature magnetized plasmas. *Journal of Physics D: Applied Physics*, 2023.
- ¹³Alberto Marín-Cebrián, Enrique Bello-Benítez, Adrián Domínguez-Vázquez, and Eduardo Ahedo. Non-maxwellian electron effects on the macroscopic response of a hall thruster discharge from an axial-radial kinetic model. *Plasma Sources Science and Technology*, 33(2):025008, 2024.
- ¹⁴V. Kim. Main physical features and processes determining the performance of stationary plasma thrusters. *J. Propulsion Power*, 14(5):736–743, 1998.
- ¹⁵M.B. Belikov, O.A. Gorshkov, R.N. Rizakhanov, A.A. Shagayda, and S.A. Khartov. Hall-type low- and mean-power thrusters output parameters. In *35th Joint Propulsion Conference, Los Angeles, CA*, AIAA-99-2571, 1999.
- ¹⁶A.I. Morozov and V.V. Savel'yev. Fundamentals of stationary plasma thruster theory. In *Reviews of Plasma Physics, Vol. 21*, New York, 2000. Kluwer Academic.
- ¹⁷Jan Miedzik, Serge Barral, and Dariusz Daniłko. Influence of oblique magnetic field on electron cross-field transport in a Hall effect thruster. *Physics of Plasmas*, 22(4):043511, 2015.
- ¹⁸Alberto Marín-Cebrián, Adrián Domínguez-Vázquez, Pablo Fajardo, and Eduardo Ahedo. Kinetic plasma dynamics in a radial model of a Hall thruster with a curved magnetic field. *Plasma Sources Science and Technology*, 31(11):115003, 11 2022.
- ¹⁹James Szabo, Noah Warner, Manuel Martinez-Sánchez, and Oleg Batishchev. Full particle-in-cell simulation methodology for axisymmetric Hall effect thrusters. *Journal of Propulsion and Power*, 30(1):197–208, 2014.
- ²⁰Jinwen Liu, Hong Li, Yanlin Hu, Xingyu Liu, Yongjie Ding, Liqui Wei, Daren Yu, and Xiaogang Wang. Particle-in-cell simulation of the effect of curved magnetic field on wall bombardment and erosion in a Hall thruster. *Contributions to Plasma Physics*, 59(8):e201800001, 2019.
- ²¹Dong Ma, Demai Zeng, Lei Wang, Yongjie Ding, Liqui Wei, Hong Li, and Daren Yu. Numerical simulation study on the influence of channel geometry on discharge characteristics of low-power magnetically shielded hall thrusters. *Vacuum*, 180:109547, 2020.
- ²²F Taccogna, F Cichocki, and P Minelli. Coupling plasma physics and chemistry in PIC model of electric propulsion: application to an air-breathing low power Hall thruster. *Frontiers*, 10:1006994, 2022.
- ²³Olivier Duchemin, Julien Rabin, Lahib Balika, Giovanni Coduti, Vanessa Vial, Daniel Vuglec, Xavier Cavelan, and Vaitua Leroi. Qualification status of the PPS-5000 Hall thruster unit. In *36th International Electric Propulsion Conference*, number IEPC-2019-906. Electric Rocket Propulsion Society, Fairview Park, OH, 2019.
- ²⁴Olivier B Duchemin, Julien Rabin, Giovanni Coduti, and David Le Méhauté. Expanding the mission capture of the PPS® 5000 Hall thruster. In *ASCEND 2023*, page 4790, 2023.
- ²⁵Alberto Marín-Cebrián, Enrique Bello-Benítez, Eduardo Ahedo, and Adrián Domínguez-Vázquez. Kinetic electron effects in a Hall thruster discharge with a curved magnetic field topology. In *38th International Electric Propulsion Conference*, number IEPC-2024-387, Toulouse, France, June 23–28, 2024. Electric Rocket Propulsion Society.
- ²⁶C.K. Birdsall and A.B. Langdon. *Plasma Physics via Computer Simulation*. Institute of Physics Publishing, Bristol, 1991.
- ²⁷A. Domínguez-Vázquez, F. Cichocki, M. Merino, P. Fajardo, and E. Ahedo. Axisymmetric plasma plume characterization with 2D and 3D particle codes. *Plasma Sources Science and Technology*, 27(10):104009, 2018.
- ²⁸Biagi, S.F. Cross sections extracted from PROGRAM MAG-BOLTZ, version 7.1 june 2004, June 2004. [Online; accessed 5-July-2021].
- ²⁹Adrián Domínguez-Vázquez, Jiewei Zhou, Alejandro Sevillano-González, Pablo Fajardo, and Eduardo Ahedo. Analysis of the electron downstream boundary conditions in a 2D hybrid code for Hall thrusters. In *37th International Electric Propulsion Conference*, number IEPC-2022-338, Boston, MA, USA, June 19–23, 2022. Electric Rocket Propulsion Society.
- ³⁰Alberto Marín-Cebrián, Adrián Domínguez-Vázquez, Pablo Fajardo, and Eduardo Ahedo. Macroscopic plasma analysis from 1D-radial kinetic results of a Hall thruster discharge. *Plasma Sources Science and Technology*, 30(11):115011, November 2021.
- ³¹E. Ahedo, J.M. Gallardo, and M. Martínez-Sánchez. Effects of the radial-plasma wall interaction on the axial Hall thruster discharge. *Physics of Plasmas*, 10(8):3397–3409, 2003.
- ³²E Bello-Benítez and E Ahedo. Stationary axial model of the Hall thruster plasma discharge: electron azimuthal inertia and far plume effects. *Plasma Sources Science and Technology*, 32(11):115011, 2023.
- ³³Davide Poli, Enrique Bello-Benítez, Pablo Fajardo, and Eduardo Ahedo. Time-dependent axial fluid model of the Hall thruster discharge and its plume. *Journal of Physics D: Applied Physics*,

- 56(41):415203, 2023.

³⁴R.D. Hazeltine and J.D. Meiss. *Plasma confinement*. Addison-Wesley, Redwood, CA, 1992.

³⁵J.J. Ramos. Fluid formalism for collisionless magnetized plasmas. *Physics of Plasmas*, 12(5):052102, 2005.

³⁶T. Charoy, T. Lafleur, A. Tavant, P. Chabert, and A. Bourdon. A comparison between kinetic theory and particle-in-cell simulations of anomalous electron transport in ExB plasma discharges. *Physics of Plasmas*, 27(6):063510, 2020.

³⁷Sierra Jubin, Andrew Tasman Powis, Willca Villafana, Dmytro Sydorenko, Shahid Rauf, Alexander V Khrabrov, Salman Sarwar, and Igor D Kaganovich. Numerical thermalization in 2d pic simulations: Practical estimates for low-temperature plasma simulations. *Physics of Plasmas*, 31(2), 2024.